JGR Solid Earth

RESEARCH ARTICLE
10.1029/2025JB031777

Preparatory Phase of Major Earthquakes During Campi Flegrei Unrest (2020–2024)

A. G. Iaccarino[1], M. Picozzi[1,2], G. De Landro[1], and D. Spallarossa[3]

[1]Department of Physics "Ettore Pancini", University of Naples Federico II, Naples, Italy, [2]National Institute of Oceanography and Applied Geophysics—OGS, Trieste, Italy, [3]DISTAV, University of Genoa, Genoa, Italy

Key Points:

- In Campi Flegrei, main earthquakes are preceded by preparatory phases with similar behavior in seismicity and deformation
- In residual strain during seismic sequences is directly proportional to the magnitude of the main earthquake of the sequence
- We built a method to predict maximum magnitude and number of events in the upcoming days using residual strain measured in the previous days

Supporting Information:

Supporting Information may be found in the online version of this article.

Correspondence to:

A. G. Iaccarino,
antoniogiovanni.iaccarino@unina.it

Citation:

Iaccarino, A. G., Picozzi, M., De Landro, G., & Spallarossa, D. (2025). Preparatory phase of major earthquakes during Campi Flegrei unrest (2020–2024). *Journal of Geophysical Research: Solid Earth*, *130*, e2025JB031777. https://doi.org/10.1029/2025JB031777

Received 11 APR 2025
Accepted 8 SEP 2025

Author Contributions:

Conceptualization: A. G. Iaccarino, M. Picozzi
Data curation: A. G. Iaccarino, G. De Landro
Formal analysis: A. G. Iaccarino, M. Picozzi
Funding acquisition: M. Picozzi, G. De Landro, D. Spallarossa
Methodology: A. G. Iaccarino, M. Picozzi
Project administration: M. Picozzi, D. Spallarossa
Resources: M. Picozzi
Software: A. G. Iaccarino, M. Picozzi
Supervision: M. Picozzi, D. Spallarossa
Validation: A. G. Iaccarino, M. Picozzi, G. De Landro, D. Spallarossa

Abstract The ongoing unrest at Campi Flegrei is posing significant challenges for hazard assessment and risk mitigation. This densely populated region has experienced more than 20,000 shallow earthquakes since 2020, driven by hydrothermal fluid accumulation beneath a mechanically strong caprock. In this work, we analyze the seismic activity characterizing the ongoing crisis, also including the magnitude Md 4.4 occurred in May 2024 in correspondence of a cumulative caldera uplift of 130 cm at the RITE GPS station. Here, we demonstrate that the joint interpretation of micro-seismicity evolution and deformation trend reveals the preparatory phase of major earthquakes. Our analysis of 20 seismic sequences from 2015 to 2024 highlights for larger earthquakes a consistent preparatory phase, with a strong correlation between deformation rates, cumulative seismic moment, and earthquake magnitudes. Residual strain, representing the difference between deformation-driven input and seismic output, emerges as a critical parameter linearly associated with the maximum earthquake magnitudes. Unveiling the preparation phase of larger earthquakes in the densely populated Campi Flegrei area has the potential to significantly contribute to seismic risk mitigation. Preliminary, simple predictive models based on strain dynamics show promising results, leading the way to developing novel approaches to forecast earthquake magnitudes and event rates days in advance. Our insights provide a crucial foundation for improving seismic risk mitigation strategies at Campi Flegrei and other volcanic systems worldwide.

Plain Language Summary Campi Flegrei, a highly populated volcanic area near Naples, has experienced over 20,000 small earthquakes since 2020 due to underground fluid pressure. This study shows that by tracking ground movement and minor tremors, it's possible to identify signs that a larger earthquake may be approaching. Here, we found that the buildup of underground strain—stress that hasn't yet caused a quake—is closely linked to the strength of future earthquakes. These findings could help develop models to predict earthquake size and timing days in advance, improving safety in volcanic areas like Campi Flegrei.

1. Introduction

Periods of volcanic unrest, characterized by deviations in ground deformation, seismic activity, and gas emissions, represent critical windows for understanding and mitigating associated risks (Newhall & Dzurisin, 1988). But what are the implications when such unrest occurs beneath a densely populated region housing over 500,000 people (Civil Protection Department, 2019)? This pressing question arises from the ongoing unrest phase of the Campi Flegrei caldera, seismically active since 2012 (Giudicepietro et al., 2025), which affects the outskirts of Naples and Pozzuoli in southern Italy.

Spanning approximately 15 km in diameter, Campi Flegrei is Europe's largest active caldera, formed by two massive eruptions 39,000 and 14,500 years ago (Silleni et al., 2020). Following its last eruption in 1,538, the caldera entered nearly 500 years of quiescence, punctuated by multi-phase unrest since 1950, including four major uplift episodes (Del Gaudio et al., 2010; Di Vito et al., 1987, 1999). Cumulatively, these episodes have resulted in over four m of ground deformation, accompanied by intense seismic activity (Orsi et al., 1999; Tramelli et al., 2021).

Campi Flegrei caldera is a multi-hazard geological system, where key natural events—such as ground instability, earthquakes, and volcanic eruptions—interact intensively and may occur either at the same time or at different intervals, through processes of either mutual or independent (De Landro, Vanorio, Muzellec, Russo, et al., 2025).

The current unrest has raised critical challenges for scientists and civil protection authorities. Long-term projections suggest the potential for a future eruption (Kilburn et al., 2017, 2023), while daily risks include shallow

Visualization: A. G. Iaccarino, M. Picozzi, G. De Landro
Writing – original draft: A. G. Iaccarino, M. Picozzi, G. De Landro, D. Spallarossa
Writing – review & editing: A. G. Iaccarino, M. Picozzi, G. De Landro, D. Spallarossa

earthquakes that directly endanger the population (Iervolino et al., 2024). Since 2020, over 20,000 shallow earthquakes have been recorded, with magnitudes rarely exceeding M 3. Despite their modest size, their shallow depths (2–3 km) have caused significant ground shaking, particularly in Pozzuoli and Naples, generating widespread concern among residents and emergency responders (Iervolino et al., 2024; Ricci et al., 2013).

This study investigates the seismic hazards of Campi Flegrei by analyzing the preparatory phases of 20 larger earthquakes (2015–2024). Despite it is well established the link between deformation and seismicity (e.g., among many, Kilburn et al., 2023), here we present novel insights into the relationship between ground deformation rates and volcano-tectonic seismicity, providing new perspectives on the caldera's dynamics. In particular, we innovatively show that integrating deformation and seismicity data could potentially enable the prediction of earthquake magnitudes days in advance.

The origin of bradyseism remains a topic of debate (Astort et al., 2024; Troise et al., 2019). Many studies link the historical cycles of the bradyseism to cycles of both magmatic and hydrothermal activities (Bodnar et al., 2007; Lima et al., 2009, 2021). The prevailing hypothesis for the actual unrest attributes these earthquakes to the building up in pressure caused by hydrothermal fluids sealed by the shallow caprock (De Landro, Vanorio, Muzellec, Russo, et al., 2025). In recent work, De Landro, Vanorio, Muzellec, Russo, et al. (2025), leveraging precise relocations of extensive seismicity since 2014, obtained high resolution 3D tomographic images of the inner caldera which, combined with a rock physics experiment, allowed to precisely reconstruct the gas-rich reservoir below 2 km depth (Calò & Tramelli, 2025). This active hydrothermal volume interacts with a mechanically strong caprock layer (1–2 km depth), likely formed through limewater-pozzolana reactions (Vanorio et al., 2005; Vanorio & Kanitpanyacharoen, 2015). The b-value analysis made by Tramelli et al. (2024), whereas this parameter is considered a proxy of stress, confirm higher stress/strain concentration (i.e., lower b-value) in the caprock and for the deepest seismicity, while higher b-value are observed for portion of the caldera interested by volcanic gases moving toward the surface. The reservoir extent closely correlates with the area of maximum uplift, where deformation acceleration due to pore-fluid pressure is corroborated by laboratory experiments suggesting that the interaction between the pressurized gas reservoir and the confining caprock seal drives the ground uplift. At a greater depths, structural studies identify a melt-rich zone at ∼7.5 km depth (Zollo et al., 2008) and persistent CO_2 surface degassing (Caliro et al., 2025; Chiodini et al., 2015), feeding, together with the meteoric water (Vanorio et al., 2025), the entire hydrothermal and volcanic system.

The accumulation of hydrothermal fluids beneath the caprock has driven the ongoing ground uplift since 2005 (Bevilacqua et al., 2022; De Landro, Vanorio, Muzellec, Russo, et al., 2025; Kilburn et al., 2023). This deformation increases stress on pre-existing faults, triggering seismic activity. While the largest recorded event (Md 4.6) occurred in March 2025, studies of fault segments suggest that a magnitude 5 earthquake remains a plausible worst-case scenario (Iervolino et al., 2024; Scotto di Uccio et al., 2024). Verifying the existence and understanding the mechanisms of the preparatory phase of larger earthquakes is therefore an urgent necessity.

Despite well-established links between deformation and seismicity have been proposed, predictive models for the larger seismic activity posing the population at risk remain underdeveloped.

By analyzing seismicity preceding 20 major events, we identify common patterns in the preparatory phases, which for all sequences are characterized by a marked correlation between deformation rates, the seismic moment release and the main earthquake magnitudes. Notably, we observe a shift in strain dynamics from 2022, marked by a progressive increase in residual strain that correlates with larger event magnitudes.

Our findings reveal critical aspects of Campi Flegrei's seismic behavior, which can be interpreted considering the caprock's role in stress distribution. The observed linear relationship between residual strain and earthquake magnitude paves the way for forecasting methodologies. These approaches could predict the magnitude of major events days in advance, enhancing not only risk mitigation but also preparedness, emergency planning, and civil protection efforts at Campi Flegrei and other volcanic systems worldwide.

2. Data Set

We used a catalog of 12,399 events recorded at 21 stations of the INGV network insisting on the Campi Flegrei area. The data set extends from 1 January 2014, to 9 November 2024. We used P- and S-wave arrival times, along with magnitude estimates, from the INGV earthquake catalog (Ricciolino et al., 2024). This data set includes approximately 92,472 P-wave and 37,293 S-wave phases, with magnitudes ranging from −1.1 to 4.4. On average,

each event had 7–8 P-wave arrival times and 3–4 S-wave arrival times. The provided magnitude is the duration magnitude (Orsi et al., 1999).

2.1. Re-Localization

We used the catalog obtained in De Landro, Vanorio, Muzellec, Russo, et al. (2025). In this work, the authors performed the location with NLL-SSST (Lomax & Savvaidis, 2022), which mitigates the impact of velocity model errors on event location, and the 3D velocity P- and S-wave tomographic models. The main innovation of NLL-SSST is the use of spatially varying, source-specific station travel-time corrections (SSST) throughout a 3D volume, providing a position-dependent correction for each station and phase type. Following Scotto di Uccio et al. (2024), they iteratively generate SSST corrections using the catalog events and arrival data by reducing the smoothing distances to 20, 10, 5, and 2 km, ranging from larger than the seismic pattern size to the target sub-kilometer location precision. Then, they operated a selection based on location uncertainties (Figure S1 in Supporting Information S1), obtaining a final catalog of 9,894 high quality event locations with rms $\leq$ 0.08 s (0.03 s, on average), horizontal and vertical location errors $\leq$500 m for 85% of events and GAP $\leq$ 200 for the 90% of events.

2.2. Moment Magnitude

To convert the duration magnitude Md to Mw, we used the relation from Iervolino et al. (2024).

$$Mw = 0.26 + 0.80Md \quad (1)$$

Using Mw, we computed the completeness magnitude, Mc, using the entire-magnitude-range method (Woessner & Wiemer, 2005). For the whole catalog, we find a magnitude of completeness Mc 0.2.

The same Mc value was found by Tramelli et al. (2021, 2022) and considered costant since 2010 in the central part of the caldera, the same of main interest for this study where large earthquakes have occurred. Of course, for repeating the analyses with focus on other sectors of the Caldera, the Mc analysis should be repeated, and different data selection criteria applied.

Concerning the seismic moment, M_0, it is computed directly from Mw using the relation from Hanks and Kanamori (1979).

For next analysis, we will compute the cumulative moments on selected time-windows. The uncertainty associated to the cumulative moment is computed by using a bootstrap approach (Efron, 1992), by considering a number of random samplings with replacement equal to 10 times the amount of data in each sequence (Table 1).

2.3. Deformation Data

As Bevilacqua et al. (2024), we consider the deformation (DEF) measured by the GNSS station RITE (Figure 1a). Given the observed bell-shaped deformation pattern centered in the town of Pozzuoli, RITE can indeed be considered well representative of the deformation measured on the vertical component at all the GNSS stations.

To retrieve the data time-series in Figure 1c we used two different sources. Deformation data from 19 May 2000 to 31 December 2020 has been extracted from Bevilacqua et al. (2024). Later data have been digitally extracted from figures contained in the monthly and weekly reports compiled by Osservatorio Vesuviano (2024) using the OpenCV Python library (Bradski, 2000). Our DEF data extend from 19 May 2000, to 5 December 2024. As the data were digitally extracted, the sampling rate is variable, with an average of approximately 7 days. To homogenize the data set, the data from Bevilacqua et al. (2024) have been decimated to achieve a sampling rate of approximately 7 days.

The deformation rate (DR) is computed as the slope of the linear fit of deformation in time in the selected window. In Figure S2 of Supporting Information S1, we show the fits retrieved for the 12 sequences analyzed in the paper.

Table 1
Main Information Concerning the Main Events of the Studied Sequences

ID	Origin time	Latitude	Longitude	Depth (km)	Magnitude	Number of events	100-day M_{max}
1	07/10/2015 09:10:51	40.8297	14.1487	2.38	2.5	13	2.3
2	05/07/2016 01:22:40	40.8229	14.1320	1.40	2.1	5	1.5
3	12/03/2018 14:09:06	40.8320	14.1479	2.74	2.4	35	1.4
4	18/09/2018 21:36:42	40.8313	14.1461	2.50	2.5	23	1.6
5	15/03/2019 04:26:42	40.8287	14.1512	2.26	2.5	25	1.0
6	05/10/2019 05:08:38	40.8301	14.1490	2.15	2.5	23	1.7
7	06/12/2019 00:17:24	40.8296	14.1505	2.29	3.1	60	2.5
8	26/04/2020 02:59:03	40.8304	14.1502	2.51	3.3	37	2.7
9	19/12/2020 21:54:57	40.8362	14.1472	1.23	2.7	146	1.9
10	31/03/2021 23:10:50	40.8003	14.1153	4.00	2.2	113	2.6
11	06/08/2021 14:51:10	40.8034	14.1133	3.98	2.2	111	2.0
12	06/01/2022 19:37:16	40.8300	14.1432	2.03	2.5	116	2.0
13	29/03/2022 17:45:32	40.8292	14.1500	2.45	3.6	178	3.5
14	30/07/2022 03:27:49	40.8271	14.1414	1.73	2.5	118	2.0
15	12/11/2022 21:37:55	40.8014	14.1166	2.04	2.7	103	2.3
16	05/02/2023 00:45:36	40.8001	14.1099	4.53	3	284	2.7
17	11/06/2023 06:44:26	40.8353	14.1066	3.92	3.6	462	3.5
18	27/09/2023 01:35:34	40.8159	14.1569	2.95	4.2	710	3.8
19	20/05/2024 18:10:04	40.8250	14.1391	2.20	4.4	1,146	3.9
20	26/07/2024 11:46:21	40.8031	14.0955	5.00	4	1,225	4.4

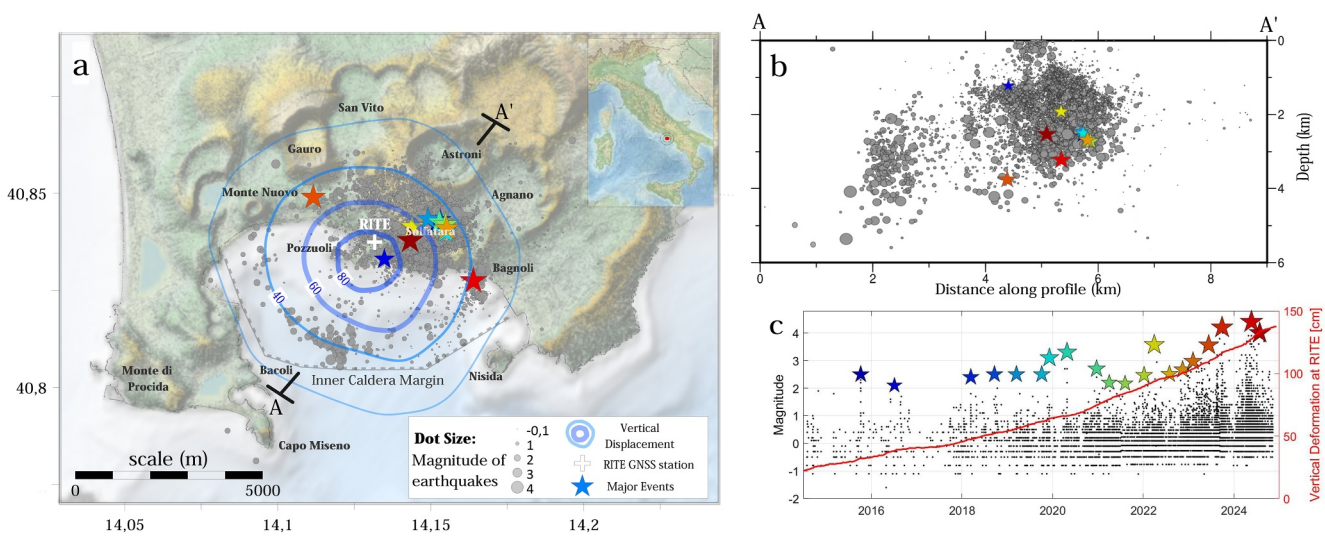

Figure 1. (a) Map of the events re-localized. The events are represented by gray circles sized by magnitude. Stars represent the location of the main events (Table 1). RITE station is represented by a white cross. The blue lines represent the vertical displacement. (b) Section of the events along the AA' segment (panel a). (c) Events and vertical deformation at RITE versus time. Events are represented as black dots with their magnitude (right *y*-axis). Colored stars represent main events (Table 1). Red line refers to the vertical displacement at RITE in cm (left *y*-axis).

3. Methods

3.1. Strain

To compute the Strain (ε), as discussed above, we consider that the deformation is due to a forcing action of hydrothermal fluids at the bottom of the caprock. We therefore assume that the entire structure above represents the body undergoing the deformation we observe at the surface. While local anelastic processes (e.g., crack opening or thermally assisted inelastic flow) may occur in the shallowest layers, their integrated contribution to the caldera-scale geodetic signal is second-order. At the caldera scale, previous studies have shown that the upper crust exhibits a quasi-elastic response to loading, indicating that the observed uplift and associated seismicity are not dominated by irreversible inelastic processes (Bevilacqua et al., 2024). Moreover, the existence of a mechanically competent fibrous caprock overlying the hydrothermal fluids reservoir (De Landro, Vanorio, Muzellec, Russo, et al., 2025; Vanorio et al., 2025; Vanorio & Kanitpanyacharoen, 2015) supports our assumption, is the ratio between DEF and the depth of the lower bound of the caprock, L = 3 km (Vanorio & Kanitpanyacharoen, 2015).

$$\varepsilon_{zz} = \frac{\mathrm{DEF}}{L} \tag{2}$$

Since the vertical deformation, near RITE, is the main contributor to the strain (Bevilacqua et al., 2022), we simply assume that

$$\varepsilon = \varepsilon_{zz} \tag{3}$$

This assumption is justified near RITE since it is the closest station to the maximum of vertical displacement in the region (Figure 1a), elsewhere, the radial component of the deformation becomes significant.

3.2. Seismic Volume

We compute the seismic volume (Vs) as the 3D convex Hull of the hypocenters in a given time window (Picozzi et al., 2023). We thus consider Vs as the part of the medium that releases stress in a certain period of time through seismicity. To compute it, we first compute the barycenter of the events and, to mitigate the impact of eventual outliers in the seismic sequences, we select a certain percentage of the closest events to compute Vs.

The choice of the percentage of events used in the analysis can significantly affect the estimation of Vs. To assess this effect, we investigated how the variability of event distances from the barycenter changes with the number of included events.

Specifically, we analyzed only those sequences containing at least 100 events, in order to get more consistent estimations. In Figure S3 of Supporting Information S1, we show, for each of these sequences, the variance of the distance from the barycenter, normalized by its maximum value, as a function of the percentage of events. The elbows of these curves indicate the portion of the sequence that is most tightly clustered around the barycenter. We identified the elbow as the point closest to the vertex (0 variance, 100% events), and found that, on average, it corresponds to 80.8% of the events. Based on this result, we decided to retain 80% of the events for the computation of Vs.

Then, we calculate the Delaunay convex hull (Delaunay, 1934) containing the selected events. Therefore, Vs will be the volume of the computed Delaunay hull. The uncertainty associated to Vs is computed by a bootstrap approach (Efron, 1992), by considering a number of random samplings with replacement equal to 10 times the number of events considered in each sequence (Table 1).

3.3. Total Strain Drop

We define the Strain Drop as the Strain that is unloaded by seismic processes. To compute the Strain Drop, we started from the definition of the seismic moment M_0 for a circular crack (Fischer & Hainzl, 2017)

$$M_{0i} = \frac{16}{7}\Delta\sigma_i \cdot r_i^3 \tag{4}$$

Where the index i refers to the ith event, $\Delta\sigma$ is the stress drop of the crack and r is its radius. It is worth to note that, the term $\frac{16}{7}$ descends from the Eshelby (1957) formulation. Even if we are in a volcanic environment, the earthquakes in the area completely resemble the tectonic ones (Iervolino et al., 2024; Scotto di Uccio et al., 2024), and we can use the above formulation.

If we assume the existence of a linear relation between stress drop and the strain drop in the form of

$$\Delta\sigma = \mu_{\text{eff}} \cdot \Delta\varepsilon \tag{5}$$

where μ_{eff} is an effective shear modulus that needs to be calculated (see Section S1 in Supporting Information S1).

Then, we can consider the cumulative of M_0 as

$$\sum_i M_{0i} = \frac{16}{7}\mu_{eff}\sum_i \Delta\varepsilon_i \cdot r_i^3 \tag{6}$$

If we assume a quasi-constant strain drop for all the events, as frequently done in literature for stress drop (Cocco et al., 2016; among others), the sum in second term can be approximated by the product of the total strain drop, $\Delta\varepsilon_{\text{tot}}$, and the seismic volume activated by all the considered events, V_S. In this way, we can write $\Delta\varepsilon_{\text{tot}}$ as

$$\Delta\varepsilon_{\text{tot}} = \frac{7}{16}\frac{\Sigma M_0}{\mu_{\text{eff}} V_S} \tag{7}$$

Also the uncertainty associated to $\Delta\varepsilon_{\text{tot}}$ is computed by a bootstrap approach (Efron, 1992).

Here, we need to find a reasonable value for μ_{eff}. We present the complete calculus in Section S1 of Supporting Information S1, however, the final result is

$$\mu_{\text{eff}} = 2\mu \cos\delta \sin\delta \tag{8}$$

Where μ is the shear modulus of the medium and δ is the dip of the fault. μ_{eff} needs, in fact, a dependence with the fault orientation since the stress drop refers to difference in shear stress on the fault. To compute μ we refer to the 1D-velocity model from Vanorio et al. (2005) and the density value from Judenherc and Zollo (2004) at 3 km depth. Using these values, we find $\mu = 9.45\ GPa$. Then, following La Rocca and Galluzzo (2019), we know that the dip distribution is not uniform in Campi Flegrei with 50% of the events having a dip between 45° and 75° with the median value around 60°. Using $\delta = 60°$, we obtain

$$\mu_{\text{eff}} = 8.19\ GPa$$

That is the value we used in this work to compute $\Delta\varepsilon_{\text{tot}}$.

3.4. Residual Strain

We define the residual strain, ε_{res}, simply as the difference between ε and $\Delta\varepsilon_{\text{tot}}$

$$\varepsilon_{\text{res}} = \varepsilon - \Delta\varepsilon_{\text{tot}} \tag{9}$$

Since error on DEF and so on ε is negligible (Bevilacqua et al., 2024), the standard error on ε_{res} will be equal to the error on $\Delta\varepsilon_{\text{tot}}$.

3.5. Fitting Procedures

In this work, we present numerous relationships, all these relations have been computed using a robust fit procedure with bisquare weight function (Dumouchel & O'Brien, 1991).

We report all the retrieved relationships in Table S1 of Supporting Information S1 with the relative Figure.

During the final preparation of this work, the corresponding author used ChatGPT in few sections of the manuscript to improve the grammar and the English and language of the paper. All of the sentences of this work, reasoning and conclusions are then original. However, after using this tool, all authors reviewed and edited the content as needed. The corresponding authors take full responsibility for the content of the published article.

4. Results

4.1. Deformation as the Driving Engine of the Preparatory Phase at Campi Flegrei

Since 2005, the Campi Flegrei caldera has undergone substantial uplift, with total ground deformation reaching approximately 135 cm from 2005 at the GPS station RITE by October 2024 (Osservatorio Vesuviano, 2024) (Figure 1c). Over the past decade, seismicity in the region has increased both in frequency and intensity, culminating in two large earthquakes, the Md 4.4 occurred on 20 May 2024 and the Md 4.6 of the 13 March 2025. This latter earthquake is not included into this study because the digital data on deformation has been extracted before its happening.

Previous studies in geothermal areas (Iaccarino & Picozzi, 2023; Picozzi & Iaccarino, 2021) proved that the analysis of seismicity prior to moderate earthquake can uncover common preparatory patterns associated with their generation. So, to explore the relationship between deformation and seismicity, we analyzed seismic data from January 2015 to November 2024, focusing on major seismic sequences that culminated in moderate earthquakes. To define these major sequences, we searched events with Md $\geq$ 2.0 that are not preceded or followed by stronger events in 60 days before and after them. In case of two events with the same magnitude closer than 60 days and both respecting the rule, we choose only the last one. This criterium lead us to define 20 major events and, subsequently, 20 major sequences that we are going to analyze in this paper (Figure 1; Table 1). Even if different criteria could have led to identify a slightly different number of sequences, we are confident of having selected as main events those that represent the peak of the seismic activity over the past years. Mignan (2012) showed that to study the preparatory processes it is necessary to have a Mc that is 2–3 order below the main events. Given that, the selection of main events with Md $\geq$ 2.0 is also related to the magnitude of completeness of our data set (Mc = 0.2). Four of these sequences (#1, #3, #7, #8) have been already analyzed by Tramelli et al. (2022) that looked at data from seismic, geodetic, and geochemical monitoring. All these sequences present a normal focal mechanism and are very close to each other in the area of Solfatara and Pisciarelli craters. Tramelli et al., found that these sequences happened along the hydrothermal system that feeds the gas emission in the surface. This area of the medium is highly fractured and saturated with geothermal gases which upward movement is limited by the caprock.

For each of the considered seismic sequences, our analyses are focused on the seismicity and deformation that occurred during the 100 days preceding each main event, while excluding the main events themselves.

We compared the seismicity of the preparatory phases, quantified through cumulative moment and event rate in the 100 days before the event, with total deformation (DEF) recorded at RITE before the main event and with deformation rate (DR) computed for the 100 days before the main. Notably, the logarithm of both event rate and cumulative moment exhibited a linear relationship with DEF and DR (Figures 2a and 2b; Figure S4 in Supporting Information S1).

These findings confirm that the seismicity leading up to the main events is not entirely stochastic but is strongly influenced by deformation and its rate. Moreover, all the analyzed sequences exhibit a consistent preparatory phase closely linked to deformation. Our results further confirm that the stress loading driving the caldera uplift modulates seismicity evolution (Bevilacqua et al., 2024; De Landro, Vanorio, Muzellec, Russo, et al., 2025; Vanorio et al., 2025), moreover, they indicate that the seismogenic processes of larger earthquakes share similar preparatory patterns.

To delve deeper into this connection from a mechanical perspective, we investigated strain (ε) and total strain drop ($\Delta\varepsilon_{tot}$) for the studied sequences, excluding the main events (Figure S5a in Supporting Information S1). While ε represents the input deformation in the system, $\Delta\varepsilon_{tot}$ captures one of its outputs—namely, seismic energy release, excluding plastic deformation, gas, and heat. We also examined residual strain (ε_{res}), defined as the difference between ε and $\Delta\varepsilon_{tot}$ (Figure S5b in Supporting Information S1), hypothesizing it as a key aspect of the caldera's energy budget.

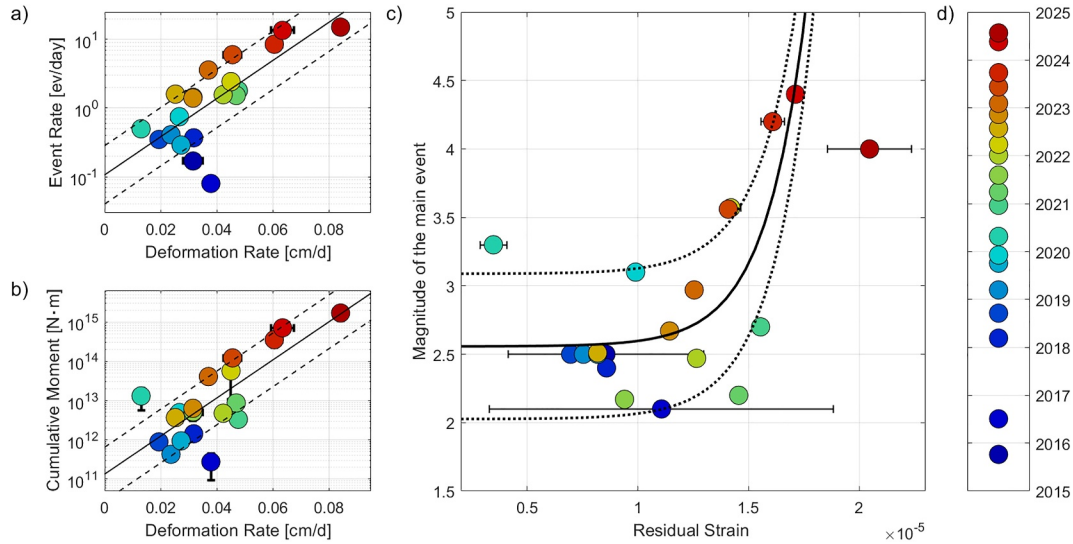

Figure 2. Different relations for the 20 main events in Table 1. Each circle refers to a single sequence, the colors of the circles are coded as in Figure 1. Black solid lines refer to the linear fit (Table S1 in Supporting Information S1). Black dashed lines refer to the $\pm\sigma$ interval for each fit. (a) Event rate versus deformation rate for all the sequences in the 100 days preceding the main event. Horizontal error bars depict the standard error on deformation rate as retrieved from the fitting procedure (see Section 3). (b) Cumulative seismic moment versus deformation rate for all the sequences in the 100 days preceding the main event. Horizontal error bars depict the standard error on deformation rate as retrieved from the fitting procedure (see Section 3). Vertical error bars depict the standard error on cumulative seismic moment as retrieved from the bootstrap analysis (see Section 3). (c) Magnitude of the main event versus residual strain for all the sequences in the 100 days preceding the main event. Horizontal error bars depict the standard error on residual strain as retrieved from the bootstrap analysis on Total Strain Drop (see Section 3).

Interestingly, ε_{res} shows an increasing relationship with the magnitude of the main event of each sequence (Figure 2c). In fact, we have been able to fit an exponential trend between ε_{res} and the magnitude of the main event using a non-linear least square algorithm and using a robust bisquare method (Dumouchel & O'Brien, 1991). This relationship points out how the magnitude of the event is critically controlled by the value of the residual strain. Despite the existence of a few outliers, we observe that for $\varepsilon_{res} \geq 13$ $\mu strain$ the main events have magnitude Md ≥ 3.0. Since events with Md ≥ 3.0 are at Campi Flegrei largely felt by population, causing distress and panic, future applications could even consider the residual strain threshold $\varepsilon_{res} = 13$ $\mu strain$ as an attention value for an alert system aiming to mitigate the seismic risk during sequences.

As reported above, we also observe in Figure 2c four seismic sequences (#8, #9, #10, #20, Table 1) behaving as outliers with respect to this relationship. Interestingly, the first three sequences are consecutives in our analysis, but we believe this as a pure coincidence being that they behave very differently from each other. The first sequence (#8) occurred in April 2020. It presents a main magnitude that is bigger than expected from ε_{res}. Interestingly, this is the only sequence characterized by a negative deformation rate (Figure S6 in Supporting Information S1). This sequence thus represents a clear exception to the empiric rule by which "high magnitude events happen during high deformation rate periods" and so, does not come as a surprise that this sequence behaves different from the others. Sequences #9 and #10, on the other hand, present a main magnitude lower than expected from ε_{res}. A possible explanation for sequence #9, happened in December 2020, is that the main event is, in fact, a doublet being it preceded by another event Md 2.7 by only 4 s. We can see these two close events as a single one and sum their seismic moment, which by using Equation 1 leads to and equivalent magnitude equal to Md 3.0. This equivalent event would now correspond to the lower confidence bound of Equation S3 in Supporting Information S1 (Figure 2c; Table S1 in Supporting Information S1). Sequence #10, which happened in March 2021, acts as outlier for all the relations for the main magnitude that we further analyze (Figure S7 in Supporting Information S1). In the end, sequence #20, happened in July 2024, the last of our data set, ended with one of the biggest event (Md 4.0), however, the relation in Figure 2c strongly overestimates its magnitude since this event happened in a period with very high residual strain. The results for sequences #10 and #20 hint us that these sequences prepared, in many aspects,

as sequences capable of generating a greater event but failed for reasons that are outside of the scopes of this paper but that will be investigated in more detail in future works.

The relationship between ε_{res} for the precursory seismicity and the magnitude of the main event suggest that as the forcing increases (e.g., through greater deformation), the amount of energy released seismically also increases, providing valuable insights into the dynamics of Campi Flegrei.

4.2. Unveiling the Preparatory Mechanisms of Seismicity at Campi Flegrei

4.2.1. The Deformation Drives the Seismicity

Our interpretation of the dynamic behavior of the Campi Flegrei caldera during the ongoing unrest phase is based on the temporal evolution of the seismicity during the preparatory phases preceding 20 major seismic events. These insights build upon foundational achievements in prior research (Bevilacqua et al., 2022; De Landro, Vanorio, Muzellec, Russo, et al., 2025; Kilburn et al., 2023) and, in turn, provide a crucial framework for advancing future studies.

We observed consistent patterns among the seismic sequences since 2015, indicating a shared preparatory mechanism underlying most of the larger earthquakes of the area (Figure 2). Expanding on earlier studies linking seismicity and deformation rates (Bevilacqua et al., 2024; Kilburn et al., 2023), our analysis introduces a novel correlation between the magnitude of these main events and the residual strain during the preparatory phases (Figure 2c, Figure S7 in Supporting Information S1). Residual strain (ε_{res}) represents the difference between the strain (ε) derived from caldera uplift and the total strain drop ($\Delta\varepsilon_{tot}$) inferred from the seismic properties of precursor earthquakes.

Interestingly, Vanorio et al. (2025; among others), by comparing the ongoing unrest (2011–2024) with the 1982–1984 episode, identifies recurring temporal patterns in seismicity and deformation, as well as consistent spatial correlations in velocity anomalies within the central caldera. In this framework, the similar preparatory patterns observed across individual seismic sequences can be interpreted as local expressions of the broader cyclic behavior characterizing the caldera unrest.

Our findings confirm that the deformation is the primary driver of seismicity during the preparatory phase. Specifically, we demonstrate that seismic output from the crustal system is directly proportional to deformation input; the maximum magnitude of each sequence scales with the preceding deformation rate (Figure S7b in Supporting Information S1). Interestingly, when considering the long-term trend, the seismicity results better visually correlated with deformation rate (Figure S6 in Supporting Information S1) than with deformation (Figure 1c).

4.2.2. Transition in Medium Behavior From Strain Drop to Strain Ratio

The temporal evolution of the ratio between total strain drop and strain ($\Delta\varepsilon_{tot}/\varepsilon$) across the 20 seismic sequences provides further insights into the caldera's dynamics (Figure 3a). In this semilog plot, it is easy to see that the strain ratio presents three periods of variation. The first consists only in the first two sequences #1 and #2, these two present high values of $\Delta\varepsilon_{tot}/\varepsilon$ probably due to a limited number of precursory earthquakes (Table 1) that leads too poor estimations of seismic volume (Vs; see Methods) and, therefore, of $\Delta\varepsilon_{tot}$. The second period goes fro 2018 to middle 2022, here the strain ratio is mostly constant around 0.01 but for sequences #7, #8 and #13 that present higher values. Then, from 2022, we have linear increase that would indicate an exponential trend. Since the first period, if exists, consists in only two values, we can not fit it properly so we fitted a piece-wise linear trend with one breakpoint using a robust bisquare method (Dumouchel & O'Brien, 1991) to fit the single linear branch and the Nelder-Mead simplex method (Lagarias et al., 1998) to find the best breakpoint that minimize the sum of RMSE of the two fits.

Our results indicate a negative trend for $\Delta\varepsilon_{tot}/\varepsilon$ until the 30 July 2022 (breakpoint date in Figure 3a), then, $\Delta\varepsilon_{tot}/\varepsilon$ clearly increases. Interestingly, if we, arbitrarily, exclude #1 and #2, from the fit, we obtain constant line for the first period and almost the same breakpoint (Figure S8 in Supporting Information S1). The retrieved breakpoint identifies a clear change in behavior of $\Delta\varepsilon_{tot}/\varepsilon$ and it results aligned with recent studies based on event rates (Bevilacqua et al., 2024; Kilburn et al., 2023). As said, sequences #7, #8 and #13 represents outliers with respect the trend in the first period, especially when we exclude sequences #1 and #2. Interestingly, these 3 sequences

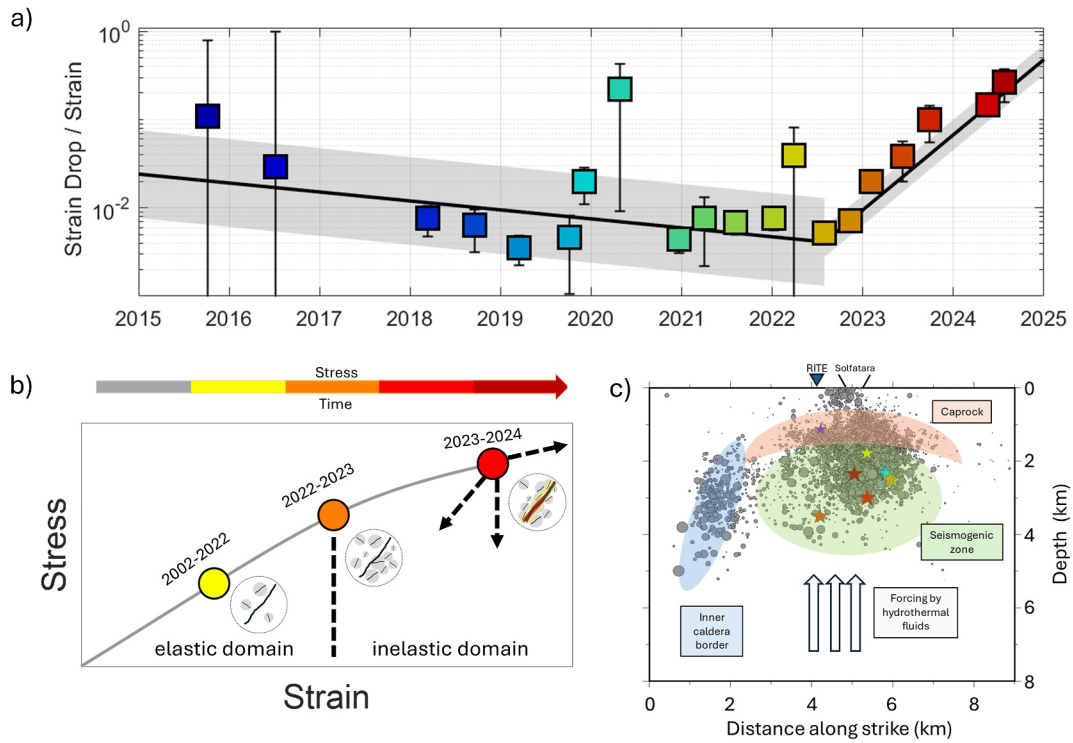

Figure 3. (a) Ratio between total strain drop and strain versus time for each sequence computed for the 100 days before the main event. The vertical black error bars associated with data represent their uncertainty. The black bold line refers to the piece-wise linear fit (Table S1 in Supporting Information S1) while the gray area represents the confidence interval of the fit. (b) Diagram of stress versus strain in time. Each colored circle refers to a different state of the system. Yellow circle, the system follows a perfect elastic behavior, in the orange circle the system enters a non-elastic phase, and at the red circle corresponds a more inelastic phase. The gray-edged circles show the state of the system schematized as a single main fault (black curve inside the circle), from right to left, the state of the system goes from a quiet state with few uncoherent off-fault structures (gray circles) to a damaged state in which the off-fault structures become well-oriented and the main fault becomes more prone to be activated. (c) Section of the events along the AA' segment (Figure 1a) with schematization of the caldera. The events are represented by gray circles sized by magnitude. Stars represent the location of the main events (Table 1). Orange area refers to the caprock. Green area corresponds to the gas reservoir. Blue area refers to the offshore inner caldera border.

represent the peaks in magnitude in their respective periods (April 2020 and March 2022, Figure 1c). Therefore, it is possible that these outliers represent smaller periods of exponentially increasing $\Delta\varepsilon_{tot}/\varepsilon$ as observed from August 2022. Unfornately, it is not possible to prove this statement yet, since there are two few points to fit any other trend, but future studies will investigate this issue.

Following the works of Kilburn et al. (2017, 2023), ε can be directly linked to the elastic response of the system, while $\Delta\varepsilon_{tot}$ is the seismic response of the system. Our results reveal a transition in the system behavior in 2021 (Figure 3b) from a quasi-elastic to a plastic-elastic (according to Kilburn et al., 2017, 2023). This transition has significant implications, since we believe it helps explaining the progressive increase in maximum earthquake magnitudes over time that we are witnessing during the ongoing crisis.

Mechanically, the stress-strain curve area corresponds to the energy per unit volume, E_v, accumulated by the system. Indeed, the product of stress, σ, and strain, ε, which corresponds to the area under the stress-strain curve, is dimensionally an energy per unit volume, E_v.

$$\sigma \cdot \varepsilon = \left[\frac{N}{m^2}\frac{m}{m}\right] = \left[\frac{J}{m^3}\right]$$

We can thus define the dependence of E_v with the increment of σ for the elastic and inelastic domain.

For the elastic domain we have

$$E_v = \int \varepsilon \, d\sigma = \int \frac{\sigma}{k} \, d\sigma \rightarrow \; E_v \propto \frac{\sigma^2}{2k} \tag{10}$$

where k represents a generic elastic constant.

While for inelastic domain, if for instance we assume an exponential relationship, Ev is

$$E_v = \int \varepsilon \, d\sigma = \int e^{\sigma k^{-1}} \, d\sigma \rightarrow \; E_v \propto k e^{\sigma k^{-1}} \tag{11}$$

In the elastic regime, strain energy accumulates quadratically with stress ($E_v \propto \sigma^2$). In contrast, in the inelastic regime, stress increments lead to exponential strain energy accumulation ($E_v \propto e^{\sigma}$). It is worth noting that earth-science-focused works explored different model for the stress and strain relation in inelastic regimes, and we made our assumption following Kilburn et al. (2023), which observed the seismicity increasing exponentially with strain in the quasi-elastic regime, then linearly in the inelastic regime. Therefore, Equation 11 is used as one simple working hypothesis to show that whatever other stress–strain (σ–ϵ) constitutive law than the linear elastic would imply larger stored strain energy for the same deformation amount.

Since co-seismic strain drop is proportional to stored strain energy (Kanamori & Brodsky, 2004), the caldera's transition to inelastic behavior enables the release of higher seismic energy, resulting in larger-magnitude earthquakes. The transition from the elastic to the inelastic domain has therefore the effect of significantly increasing the amount of E_v stored into the system, enabling the release of higher energy, mostly seismic.

Our findings align with prior interpretations of the ongoing unrest (Bevilacqua et al., 2024). Although uncertainties remain regarding the internal structure and driving forces of the unrest, a simplified model of the system captures key dynamics. Following De Landro, Vanorio, Muzellec, Russo, et al. (2025), we schematize the entire caldera volume in three primary zones (Figure 3c): the caprock, the gas-reservoir (GR), and the inner caldera border. The time-changing pressure field of the gas-enriched reservoir acting on the overlying fibrous microstructure of the caprock, is the key element driving the Earth's surface ground deformation and, consequently, triggering the occurrence of seismic sequence, first within the gas volume itself and, then, along pre-existing inner caldera bordering faults (De Landro, Vanorio, Muzellec, Russo, et al., 2025; Vanorio et al., 2025).

The current unrest, initiated in 2005, began with a slow deformation rate that allowed the GR to accommodate stress through low seismicity and small-magnitude events, occurring mostly within the caprock (De Landro, Vanorio, Muzellec, Russo, et al., 2025). As deformation accelerated, smaller fault structures in the GR began to lock, concentrating deformation on larger structures and intensifying seismicity. Until 2021, the system exhibited a near-linear stress-strain relationship. However, after surpassing the deformation levels of the 1984 bradyseism (Kilburn et al., 2023), the system entered the inelastic domain, characterized by a nonlinear stress-strain curve. This transition marked an increase in energy accumulation per unit volume, reflected in the growing magnitude of major events (Figure 3a).

Recent studies corroborate this shift from quasi-elastic to plastic-elastic behavior (Kilburn et al., 2017, 2023). By integrating geodetic and seismic data, we have uncovered critical aspects of the caldera's dynamic behavior, paving the way for refined seismic hazard assessments and offering the opportunity to test whether the evolution of seismic sequences can be used to anticipate the magnitude of future large earthquakes at Campi Flegrei.

4.3. Is It Foreseeable That the Magnitude of the Next Major Event Becomes Predictable?

Predicting earthquakes remains the ultimate challenge in seismology, and the answer to the question, "Can we predict location, magnitude and date of the next major event?" has traditionally been a definitive no. However, studies such as Rouet-Leduc et al. (2017) and subsequent research have demonstrated that, in controlled laboratory settings, the occurrence of major events can indeed be reasonably well predicted. Recent retrospective analyses of the seismicity before large tectonic earthquakes have shown that studying the collective spatial patterns and source properties of earthquakes it is possible, at least in some cases, to get hints of the proximity to a large rupture (e.g., Núñez-Jara et al., 2025; Picozzi et al., 2023, 2024a, 2024b; Venegas-Aravena &

Zaccagnino, 2025; Zaccagnino et al., 2024). Moreover, many studies on induced seismicity showed that it is possible to forecast the occurrence and the magnitude of the earthquakes using data from the fluid-injection (Langenbruch et al., 2018, 2024; Li et al., 2021; Shapiro et al., 2010, 2011). Laboratory experiments and induced seismicity scenarios where the generation of larger ruptures is driven by repeated processes are indicating that in such contexts the forecasting of magnitude of forthcoming major events is no longer an unattainable target. The case of induced seismicity is particularly interesting because it represents a scenario similar to that of Campi Flegrei, where seismicity is also related to fluid injection, though from below and not human-controlled (Akande et al., 2021).

Our aim here is thus to show that unveiling the mechanisms driving the preparatory phase of larger earthquakes at Campi Flegrei during the bradyseism represents a first step in the direction of, 1 day, predicting large earthquakes and stimulate further research in the field of earthquake prediction and forecasting. The following preliminary results that we are showing are obtained with a simple approach on purpose, in order to show the potential of studying the preparatory phases to predicting the magnitude of the next major event in the next few days. Future studies will explore the potential of artificial intelligence approaches to accomplish such a goal. It is important to note that, in this paper, we use the term "prediction" to differentiate from what the scientific community call "earthquake forecasting" because, at this preliminary stage, we do not introduce any probability assessment (Kagan, 1997; Kagan & Knopoff, 1987).

As we have shown, at Campi Flegrei, the magnitude of the next large earthquake, M_{max}, is closely tied to the energy per unit volume accumulated during stress loading. Consequently, M_{max} is linearly related to parameters such as total deformation (DEF), deformation rate (DR), cumulative seismic moment, and residual strain (ε_{res}) (Figure 2c; Figure S7 in Supporting Information S1). These relationships suggest the potential to develop a methodology for predicting the magnitude of the next major event at Campi Flegrei. Besides the maximum magnitude, we also explore the possibility of predicting the seismic rate.

4.3.1. Prediction Procedure

Here, we will not only focus on the sequences in Table 1, but we will use the whole data set of 12,399 events. The new analysis includes two steps: (a) We set a training period within which a moving temporal window is characterized by the measured residual strain, ε_{res}, and this latter put in relation with the maximum magnitude (or the number of events) within another time window in the future; (b) Then, for the testing phase, we use the relation obtained from step 1 (the training set) and the ε_{res} estimates for a given time window to predict the maximum magnitude (or the number of events) in the future.

The data set until 3 October 2023 (day after the last Md 4.0 event of 2023) is used as a training set. Data from 3 October 2023, which clearly have not be used during the training, are used as a testing set. All the quantities are computed every day at midnight, so that we obtain one set of data every day. It is worth mentioning, that after having done preliminary analyses with different paramters, we have identified ε_{res} as the most promising one for constructing the prototype of predictive system.

Furthermore, it is also worth to specify that we have trained two different models, both having ε_{res} as input, but in one case the maximum magnitude, M_{max}, as output and logarithm of the number of events, LN_{ev} in the other one. Moreover, we compute ε_{res} on a causal moving window (only data in the past) with the length of NN days, while M_{max}, and LN_{ev} are computed on an anti-causal moving window (only data in the future) with the length of MM days.

When we relate ε_{res} with M_{max} and LN_{ev} (Figures 4a, 4c, 5a, and 5c) for the whole testing period using different time windows and binned data, we observe that their relation can be reasonably approximated by linear relationships. We therefore explore different time window dimensions over the testing period to optimize the prediction capability of the linear models between ε_{res} and M_{max} or LN_{ev}. The fits are computed binning the data by M_{max}, and LN_{ev}, in order to weight evenly the days with low and with high activity (that are naturally scarcer). Moreover, for LN_{ev} prediction, we do not bin days with less than 10 events, that are not in the interest of the methodology and may wrongfully force the relation. In the end, the prediction is made using a linear relationship obtained with a robust fit with bisquare weight function (Dumouchel & O'Brien, 1991).

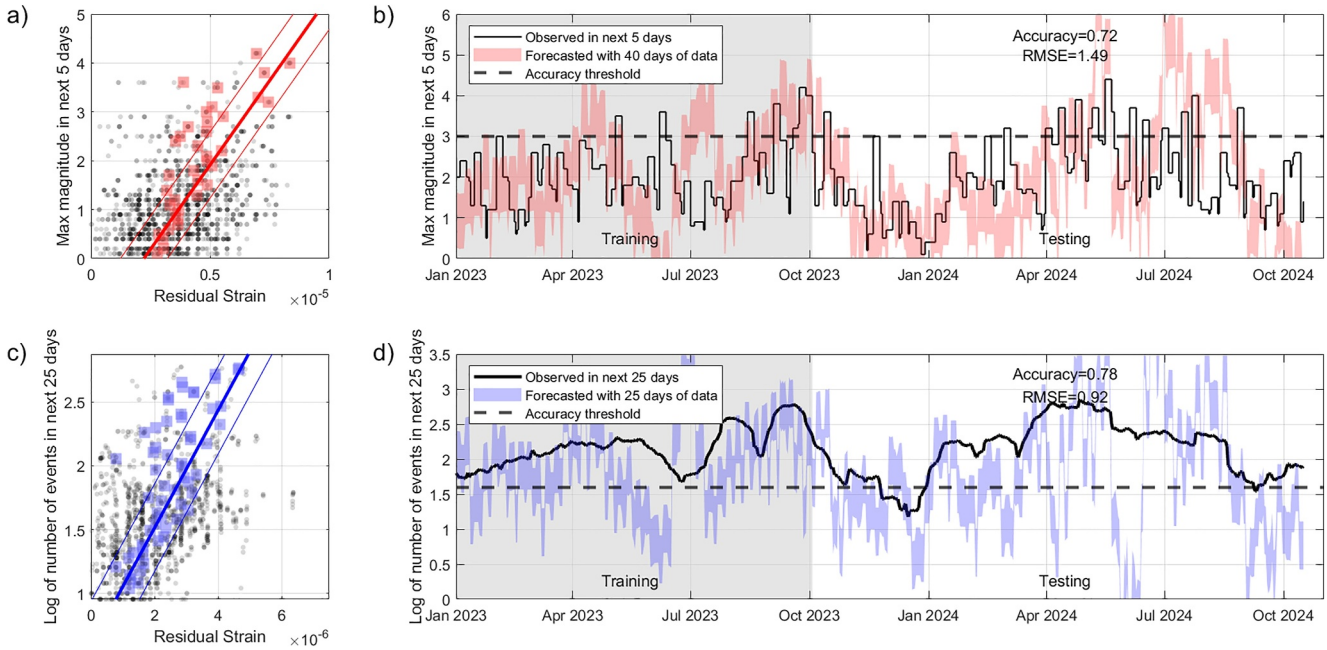

Figure 4. Best models for prediction of Mmax and LNev selected by accuracy (Figure S8 in Supporting Information S1). (a) Maximum magnitude recorded in the next 5 days versus Residual Strain measured in the last 40 days. Black shaded dots refer to daily data. Red shaded squares refer to data binned in along the *y*-axis. Red solid lines refer to the fit (Table S1 in Supporting Information S1) and to the confidence interval. (b) Prediction of the Maximum magnitude recorded in the next 5 days using data from the last 40 days. Black line represents the observed value of Maximum magnitude. The red area represents the confidence interval of the prediction. The black dashed line refers to the threshold used to compute accuracy. (c) Logarithm of number of events for the next 25 days versus Residual Strain measured in the last 25 days. Black shaded dots refer to daily data. Blue shaded squares refer to data binned in along the *y*-axis. Blue solid lines refer to the fit (Table S1 in Supporting Information S1) and to the confidence interval. (b) Prediction of the Logarithm of number of events for the next 25 days using data from the last 25 days. Black line represents the observed value of Logarithm of number of events. Blue area represents the confidence interval of the prediction. The black dashed line refers to the threshold used to compute accuracy.

We explored different values for NN and MM, from 20 to 120 days and from 5 to 60 days, respectively. In the end, we evaluate the models obtained with the training set on the testing set. We assess the methodology performance using two different statistical scores, that is to say accuracy and RMSE.

4.3.2. Prediction Results

In first instance, we use the accuracy of the prediction to select the best model. For M_{max} prediction, we define the positive cases to be the days when real $M_{max} \geq 3$ (i.e., earthquakes of public concern). For LN_{ev} prediction, we use, as threshold, the 70th percentile of real LN_{ev} in the test set, defining as positive cases the days with LN_{ev} greater than the threshold. We make this choice to avoid having combinations of NN and MM with high imbalance between positive and negative cases. We report the accuracy scores for all the models explored in Figure S9 of Supporting Information S1. We excluded from the evaluation the cases for which the relation obtained a R^2 score lower than 0.3 (gray square).

Figure 4 illustrates the best-performing models by accuracy for predicting M_{max} and LN_{ev}. As said, the model has been trained on data up to 3 October 2023 (gray area) and validated against data from October 2023 to November 2024, including the seismic sequence containing the largest recorded earthquake at Campi Flegrei within our period of study (#19, Table 1).

For M_{max}, the best model by accuracy is obtained for NN = 40, and MM = 5 with an accuracy of 0.72. The retrieved prediction equation (Figure 4a) is

$$M_{max} = (-1.54 \pm 0.33) + \left(6.90 * 10^5 \pm 0.70 * 10^5\right) * \varepsilon_{res};\ \sigma = 0.68 \quad (12)$$

Results for M_{max} are presented with ±1 standard deviation over time in Figure 4b. During the testing period, the model successfully captured the trend of the real M_{max} until the first days of May 2024. After it, the main event of

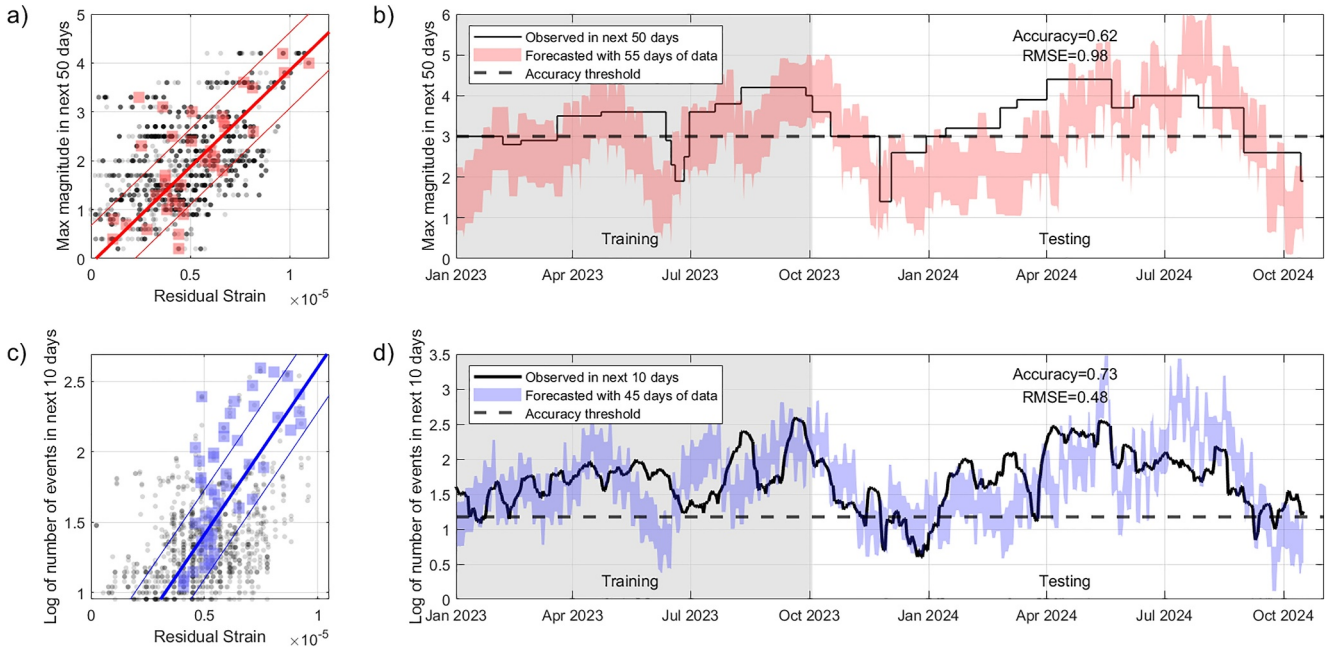

Figure 5. Best models for prediction of Mmax and LNev selected by RMSE (Figure S9 in Supporting Information S1). (a) Maximum magnitude recorded in the next 50 days versus Residual Strain measured in the last 55 days. Black shaded dots refer to daily data. Red shaded squares refer to data binned in along the *y*-axis. Red solid lines refer to the fit (Table S1 in Supporting Information S1) and to the confidence interval. (b) Prediction of the Maximum magnitude recorded in the next 50 days using data from the last 55 days. Black line represents the observed value of Maximum magnitude. The red area represents the confidence interval of the prediction. The black dashed line refers to the threshold used to compute accuracy. (c) Logarithm of number of events for the next 10 days versus Residual Strain measured in the last 45 days. Black shaded dots refer to daily data. Blue shaded squares refer to data binned in along the *y*-axis. Blue solid lines refer to the fit (Table S1 in Supporting Information S1) and to the confidence interval. (b) Prediction of the Logarithm of number of events for the next 10 days using data from the last 45 days. Black line represents the observed value of Logarithm of number of events. Blue area represents the confidence interval of the prediction. The black dashed line refers to the threshold used to compute accuracy.

sequence #19, the largest event in our records, is over-estimated. From June 2024 to July 2024, the prediction is good again while after it become quite unstable. However, the main event of sequence #20 is well-predicted.

For LN_{ev}, the best model by accuracy is obtained for NN = 25, and MM = 25 with an accuracy of 0.78. The retrieved prediction equation (Figure 4c) is

$$LN_{ev} = (0.59 \pm 0.11) + \left(4.61 * 10^5 \pm 0.43 * 10^5\right) * \varepsilon_{res};\ \sigma = 0.34 \quad (13)$$

Results for LN_{ev} are presented with ±1 standard deviation over time in Figure 4d. In this case, the model is able to characterize the general trend of the seismicity until May 2024 but the prediction is underestimated from mid-January 2024 to mid-March 2024. Despite that, the most critical period of sequence #19 (10–20 May 2024) is well-predicted. Just after the main event, the model strongly underestimates LN_{ev} for about a month. After July 2024, the model well predicts a decreasing trend but the predictions become extrememely variable.

In the second method, we use RMSE. RMSE on the testing set is the best estimation for the uncertainty of the prediction and it is usually greater than the one obtained for the training set. We report the RMSE computed for all the models explored in Figure S10 of Supporting Information S1. As done before, we excluded from the evaluation the cases for which the relation obtained a R^2 score lower than 0.3 (gray square).

Figure 5 illustrates the best-performing models by RMSE for predicting M_{max} and LN_{ev}. For M_{max}, the best model by accuracy is obtained for NN = 50, and MM = 55 with an RMSE of 0.98. The retrieved prediction equation (Figure 5a) is

$$M_{max} = (-0.10 \pm 0.32) + \left(3.95 * 10^5 \pm 0.56 * 10^5\right) * \varepsilon_{res};\ \sigma = 0.78 \quad (14)$$

Results for M_{max} are presented with ±1 standard deviation over time in Figure 5b. The model is able to catch the general trend of M_{max}. In this case, the method predicts M_{max} in within 1σ almost in all the testing set but for the period between Mid-January 2024 and mid-April 2024 where the estimation is underestimated. So that, the model correctly predict M_{max} during sequences #19, well-predicting the occurrence of the main event. On the other hand, the model slightly overestimates M_{max} during the occurrence of the main event of sequence #20 in July 2024.

For LN_{ev}, the best model by accuracy is obtained for NN = 45, and MM = 10 with an RMSE of 0.48. The retrieved prediction equation (Figure 5c) is

$$LN_{ev} = (0.23 \pm 0.29) + \left(2.37 * 10^5 \pm 0.47 * 10^5\right) * \varepsilon_{res};\ \sigma = 0.32 \quad (15)$$

Results for LN_{ev} are presented with ±1 standard deviation over time in Figure 5d. The model well predicts LN_{ev} until mid-January. After that, the model predicts the general increasing trend underestimating the real values until May 2024. After May 2024, the model, most of the time, well predicts or slightly overestimates LN_{ev}. During the main events of both sequences #19 and #20, LN_{ev} is slightly overestimated.

4.3.3. Take-Away Messages From Prediction Procedure

We introduced a prototype approach for the prediction of M_{max} and LN_{ev} using seismological and deformation data in Campi Flegrei. We explored many configurations of parameters looking for the best model. However, how to select the best model is a not trivial problem. As seen, many models achieve good results in the prediction so it is reasonable to believe that many models can be seen as the best model depending on the score chosen to judge the models. So that, the choice of the score is a key aspect.

For example, choosing accuracy, as done for Equations 10 and 11 (Figure 4), we prefer to use a model that predicts the a binary output and that answers the question "will the M_{max} be greater than 3.0?" or similar for LN_{ev}. This kind of models can be very useful for emergency managent where usually it is used some sort of threshold to declare alerts or to raise alert levels. On the other hand, choosing RMSE, we prefer models that overall predict the exact values of the output. These models are usually preferable but not always achievable since the problem can be too complex. So that, the models themselves tend to be more complex and so, more prone to overfitting failing to predict new data.

The retrieved models (Equations 10–13) are able to generally catch the trends of M_{max} and LN_{ev} even if they fail, in certain periods, in correctly predicting the exact value. We believe that, the models ability to catch the general trend of seismicity hints that the problem is solvable, so that M_{max} and LN_{ev} are effectively dependent on the seismicity and deformation in the previous days. This also suggests that at the bradyseism is characterized by cycles of pressure buildup and seismicity that make the system almost predictable. On the other hand, the fact that all the models fail to predict certain periods suggests that more complex models are needed or that ensembles of simpler models is needed to achieve better performances.

It is interesting to note that most of the events in our data set are located in the central area below Solfatara crater. This can be a reliability factor for the models, since the effective location of the events is never taken into account, except for the computation of Vs. We believe that, in future works, further improvements could be achieved taking to account the events location.

5. Conclusions

In this work, we studied the preparatory phase of major earthquakes in Campi Flegrei exploring the link between deformation and seismicity. Our findings provide transformative insights into the preparatory processes underlying seismicity at Campi Flegrei, offering a critical foundation for developing predictive models that could significantly enhance risk mitigation efforts in this densely populated area.

By elucidating the relationship between deformation and seismicity, this study advances our understanding of the dynamic behavior of Campi Flegrei and establishes a clear link between seismicity, deformation, and deformation rates. Notably, we demonstrate that major seismic events at Campi Flegrei follow a common preparatory process directly tied to deformation, revealing a cyclic behavior that holds promise for forecasting methodologies applicable to other active volcanic systems worldwide.

The integration of geodetic and seismic data reveals a significant departure from elastic behavior in the caldera's response, beginning in 2022. This transition underscores the importance of continued monitoring and model refinement to address the pressing challenges of seismic hazard mitigation.

Our results highlight the potential to anticipate major seismic events at Campi Flegrei, marking a significant step toward proactive hazard management and contributing to the development of effective early warning systems. By linking major events with their precursory seismicity, this study provides a template for broader applications in volcanic risk assessment.

While uncertainties remain regarding the caldera's internal dynamics, the demonstrated correlation between deformation patterns and seismic outcomes represents a critical advance in the pursuit of reliable earthquake forecasting. These findings emphasize the necessity of sustained observation and interdisciplinary approaches to improve risk management in volcanic regions worldwide. Translating these insights into reliable forecasting tools will require further research, long-term data, and methodological advances.

Conflict of Interest

The authors declare no conflicts of interest relevant to this study.

Data Availability Statement

The initial seismic catalogue used in this paper and the deformation data are available at the ZENODO repository by (De Landro, Vanorio, Muzellec, & Lomax, 2025). All the processed data and models presented in the paper, and the codes to produce the Figures are available at Iaccarino et al. (2025). Other data and software are available on request.

Acknowledgments

We thanks the associate editor, Dr, Yosuke Aoki, Dr. Anna Tramelli, and the anonymous reviewer for the helpful critiques and suggestions that helped improving the work. The work presented in this paper was supported by the PRIN projects: "Intercepting the PREparatory Phase of lARge earthquakes from seismic information and gEodetic Displacement" (PREPARED—Project code 2022ZHXWC9); "Relation Between 3d Thermo-Rheological Model And Seismic Hazard For The Risk Mitigation In The Urban Areas Of Southern Italy" (TRHAM—Project code P2022P37SN). This work has received financial support by the "Multi-Risk sciEnce for resilienT commUnities undeR a changiNg climate" (RETURN) project, funded by the European Union's NextGenerationEU and the Italian Ministry of University and Research (MUR) under the National Recovery and Resilience Plan (NRRP; Code PE0000005). Open access publishing facilitated by Universita degli Studi di Napoli Federico II, as part of the Wiley - CRUI-CARE agreement.

References

Akande, W. G., Gan, Q., Cornwell, D. G., & De Siena, L. (2021). Thermo-hydro-mechanical model and caprock deformation explain the onset of an ongoing Seismo-volcanic unrest. *Journal of Geophysical Research: Solid Earth*, *126*(3), e2020JB020449. https://doi.org/10.1029/2020JB020449

Astort, A., Trasatti, E., Caricchi, L., Polcari, M., De Martino, P., Acocella, V., & Di Vito, M. A. (2024). Tracking the 2007–2023 magma-driven unrest at Campi Flegrei caldera (Italy). *Communications Earth & Environment*, *5*(1), 1–15. https://doi.org/10.1038/s43247-024-01665-4

Bevilacqua, A., De Martino, P., Giudicepietro, F., Ricciolino, P., Patra, A., Pitman, E. B., et al. (2022). Data analysis of the unsteadily accelerating GPS and seismic records at Campi Flegrei caldera from 2000 to 2020. *Scientific Reports 2022 12:1*, *12*(1), 1–24. https://doi.org/10.1038/s41598-022-23628-5

Bevilacqua, A., Neri, A., De Martino, P., Giudicepietro, F., Macedonio, G., & Ricciolino, P. (2024). Accelerating upper crustal deformation and seismicity of Campi Flegrei caldera (Italy), during the 2000–2023 unrest. *Communications Earth & Environment*, *5*(1), 1–14. https://doi.org/10.1038/s43247-024-01865-y

Bodnar, R. J., Cannatelli, C., De Vivo, B., Lima, A., Belkin, H. E., & Milia, A. (2007). Quantitative model for magma degassing and ground deformation (Bradyseism) at Campi Flegrei, Italy: Implications for future eruptions. *Geology*, *35*(9), 791–794. https://doi.org/10.1130/G23653A.1

Bradski, G. (2000). *The OpenCV library*. Dr. Dobb's Journal of Software Tools.

Caliro, S., Chiodini, G., Avino, R., Carandente, A., Cuoco, E., Di Vito, M. A., et al. (2025). Escalation of caldera unrest indicated by increasing emission of isotopically light sulfur. *Nature Geoscience*, *18*(2), 167–174. https://doi.org/10.1038/s41561-024-01632-w

Calò, M., & Tramelli, A. (2025). Evidences of the structures controlling the unrest in Campi Flegrei, Italy; Joint interpretation of ambient noise and local earthquake tomography. *Journal of Volcanology and Geothermal Research*, *457*, 108236. https://doi.org/10.1016/J.JVOLGEORES.2024.108236

Chiodini, G., Vandemeulebrouck, J., Caliro, S., D'Auria, L., De Martino, P., Mangiacapra, A., & Petrillo, Z. (2015). Evidence of thermal-driven processes triggering the 2005–2014 unrest at Campi Flegrei caldera. *Earth and Planetary Science Letters*, *414*, 58–67. https://doi.org/10.1016/J.EPSL.2015.01.012

Civil Protection Department. (2019). Update of the national emergency plan for Campi Flegrei. Retrieved from https://www.protezionecivile.gov.it/en/approfondimento/update-of-the-national-emergency-plan-for-campi-flegrei/

Cocco, M., Tinti, E., & Cirella, A. (2016). On the scale dependence of earthquake stress drop. *Journal of Seismology*, *20*(4), 1151–1170. https://doi.org/10.1007/S10950-016-9594-4/FIGURES/8

De Landro, G., Vanorio, T., Muzellec, T., & Lomax, A. (2025). Source data of "3D structure and dynamics of Campi Flegrei enhance multi-hazard assessment [Dataset]. *Zenodo*. https://doi.org/10.5281/ZENODO.15106480

De Landro, G., Vanorio, T., Muzellec, T., Russo, G., Lomax, A., Virieux, J., & Zollo, A. (2025). 3D structure and dynamics of Campi Flegrei enhance multi-hazard assessment. *Nature Communications*, *16*(1), 4814. (Accepted for Pubblication). https://doi.org/10.1038/s41467-025-59821-z

Delaunay, B. (1934). Sur la sphere vide (On the empty sphere). *Bulletin de l'Académie des Sciences de l'URSS, Classe des Sciences Mathématiques et Naturelles*, *6*, 793–800.

Del Gaudio, C., Aquino, I., Ricciardi, G. P., Ricco, C., & Scandone, R. (2010). Unrest episodes at Campi Flegrei: A reconstruction of vertical ground movements during 1905–2009. *Journal of Volcanology and Geothermal Research*, *195*(1), 48–56. https://doi.org/10.1016/J.JVOLGEORES.2010.05.014

Di Vito, M., Isaia, R., Orsi, G., Southon, J., De Vita, S., D'Antonio, M., et al. (1999). Volcanism and deformation since 12,000 years at the Campi Flegrei caldera (Italy). *Journal of Volcanology and Geothermal Research*, *91*(2–4), 221–246. https://doi.org/10.1016/S0377-0273(99)00037-2

Di Vito, M., Lirer, L., Mastrolorenzo, G., & Rolandi, G. (1987). The 1538 Monte Nuovo eruption (Campi Flegrei, Italy). *Bulletin of Volcanology*, *49*(4), 608–615. https://doi.org/10.1007/BF01079966/METRICS

Dumouchel, W., & O'Brien, F. (1991). *Integrating a robust option into a multiple regression computing environment* (Vol. 36, pp. 41–48). Institute for Mathematics and Its Applications. https://doi.org/10.1007/978-1-4613-9154-8_3

Efron, B. (1992). Bootstrap methods: Another look at the Jackknife. *Springer Series in Statistics*, 569–593. https://doi.org/10.1007/978-1-4612-4380-9_41

Eshelby, J. D. (1957). The determination of the elastic field of an Ellipsoidal inclusion, and related problems. In *Proceedings of the Royal Society of London. Series A. Mathematical and Physical Sciences* (Vol. 241(1226)). 376–396. https://doi.org/10.1098/rspa.1957.0133

Fischer, T., & Hainzl, S. (2017). Effective stress drop of earthquake clusters. *Bulletin of the Seismological Society of America*, *107*(5), 2247–2257. https://doi.org/10.1785/0120170035

Giudicepietro, F., Avino, R., Bellucci Sessa, E., Bevilacqua, A., Bonano, M., Caliro, S., et al. (2025). Burst-like swarms in the Campi Flegrei caldera accelerating unrest from 2021 to 2024. *Nature Communications*, *16*(1), 1–14. https://doi.org/10.1038/s41467-025-56723-y

Hanks, T. C., & Kanamori, H. (1979). A moment magnitude scale. *Journal of Geophysical Research B: Solid Earth*, *84*(B5), 2348–2350. https://doi.org/10.1029/JB084iB05p02348

Iaccarino, A. G., & Picozzi, M. (2023). Detecting the preparatory phase of induced earthquakes at the geysers (California) using K-Means clustering. *Journal of Geophysical Research: Solid Earth*, *128*(10), e2023JB026429. https://doi.org/10.1029/2023JB026429

Iaccarino, A. G., Picozzi, M., De Landro, G., & Spallarossa, D. (2025). Data repository for preparatory phase of major earthquakes during Campi Flegrei unrest (2020–2024) [Dataset]. *Zenodo*. https://doi.org/10.5281/ZENODO.15197108

Iervolino, I., Cito, P., De Falco, M., Festa, G., Herrmann, M., Lomax, A., et al. (2024). Seismic risk mitigation at Campi Flegrei in volcanic unrest. *Nature Communications*, *15*(1), 1–14. https://doi.org/10.1038/s41467-024-55023-1

Judenherc, S., & Zollo, A. (2004). The Bay of Naples (Southern Italy): Constraints on the volcanic structures inferred from a dense seismic survey. *Journal of Geophysical Research*, *109*(10). https://doi.org/10.1029/2003JB002876

Kagan, Y. Y. (1997). Are earthquakes predictable? *Geophysical Journal International*, *131*(3), 505–525. https://doi.org/10.1111/J.1365-246X.1997.TB06595.X

Kagan, Y. Y., & Knopoff, L. (1987). Statistical short-term earthquake prediction. *Science*, *236*(4808), 1563–1567. https://doi.org/10.1126/SCIENCE.236.4808.1563

Kanamori, H., & Brodsky, E. E. (2004). The physics of earthquakes. *Reports on Progress in Physics*, *67*(8), 1429–1496. https://doi.org/10.1088/0034-4885/67/8/R03

Kilburn, C. R. J., Carlino, S., Danesi, S., & Pino, N. A. (2023). Potential for rupture before eruption at Campi Flegrei caldera, southern Italy. *Communications Earth & Environment*, *4*(1), 1–12. https://doi.org/10.1038/s43247-023-00842-1

Kilburn, C. R. J., De Natale, G., & Carlino, S. (2017). Progressive approach to eruption at Campi Flegrei caldera in southern Italy. *Nature Communications*, *8*(1), 1–8. https://doi.org/10.1038/ncomms15312

Lagarias, J. C., Reeds, J. A., Wright, M. H., & Wright, P. E. (1998). Convergence properties of the Nelder-Mead simplex method in low dimensions. *SIAM Journal on Optimization*, *9*(1), 112–147. https://doi.org/10.1137/S1052623496303470

Langenbruch, C., Moein, M. J. A., & Shapiro, S. A. (2024). Are maximum magnitudes of induced earthquakes controlled by pressure diffusion? *Philosophical Transactions of the Royal Society A: Mathematical, Physical and Engineering Sciences*, *382*(2276), 20230184. https://doi.org/10.1098/rsta.2023.0184

Langenbruch, C., Weingarten, M., & Zoback, M. D. (2018). Physics-based forecasting of man-made earthquake hazards in Oklahoma and Kansas. *Nature Communications*, *9*(1), 1–10. https://doi.org/10.1038/s41467-018-06167-4

La Rocca, M., & Galluzzo, D. (2019). Focal mechanisms of recent seismicity at Campi Flegrei, Italy. *Journal of Volcanology and Geothermal Research*, *388*, 106687. https://doi.org/10.1016/J.JVOLGEORES.2019.106687

Li, Z., Elsworth, D., Wang, C., Boyd, L., Frone, Z., Metcalfe, E., et al. (2021). Constraining maximum event magnitude during injection-triggered seismicity. *Nature Communications*, *12*(1), 1–9. https://doi.org/10.1038/s41467-020-20700-4

Lima, A., Bodnar, R. J., De Vivo, B., Spera, F. J., & Belkin, H. E. (2021). Interpretation of recent unrest events (Bradyseism) at Campi Flegrei, Napoli (Italy): Comparison of models based on cyclical hydrothermal events versus shallow magmatic intrusive events. *Geofluids*, *2021*(1), 2000255. https://doi.org/10.1155/2021/2000255

Lima, A., De Vivo, B., Spera, F. J., Bodnar, R. J., Milia, A., Nunziata, C., et al. (2009). Thermodynamic model for uplift and deflation episodes (Bradyseism) associated with magmatic–hydrothermal activity at the Campi Flegrei (Italy). *Earth-Science Reviews*, *97*(1–4), 44–58. https://doi.org/10.1016/J.EARSCIREV.2009.10.001

Lomax, A., & Savvaidis, A. (2022). High-precision earthquake location using source-specific station terms and inter-event waveform similarity. *Journal of Geophysical Research: Solid Earth*, *127*(1), e2021JB023190. https://doi.org/10.1029/2021JB023190

Mignan, A. (2012). Seismicity precursors to large earthquakes unified in a stress accumulation framework. *Geophysical Research Letters*, *39*(21), 21308. https://doi.org/10.1029/2012GL053946

Newhall, C. G., & Dzurisin, D. (1988). *Historical unrest at the large calderas of the world (Issue 1855)*. Department of the Interior, US Geological Survey.

Núñez-Jara, S., Martínez-Garzón, P., Kwiatek, G., Ben-Zion, Y., Dresen, D., Becker, D., et al. (2025). Unraveling the spatiotemporal fault activation in a complex fault system: The run-up to the 2023 MW 7.8 Kahramanmaraş earthquake, Türkiye. *Earth and Planetary Science Letters*, *669*, 119570. https://doi.org/10.1016/j.epsl.2025.119570

Orsi, G., Civetta, L., Del Gaudio, C., De Vita, S., Di Vito, M. A., Isaia, R., et al. (1999). Short-term ground deformations and seismicity in the resurgent Campi Flegrei caldera (Italy): An example of active block-resurgence in a densely populated area. *Journal of Volcanology and Geothermal Research*, *91*(2–4), 415–451. https://doi.org/10.1016/S0377-0273(99)00050-5

Osservatorio Vesuviano. (2024). *Bollettini di sorveglianza dei vulcani campani. Osservatorio Vesuviano*. Istituto Nazionale Di Geofisica e Vulcanologia (INGV).

Picozzi, M., & Iaccarino, A. G. (2021). Forecasting the preparatory phase of induced earthquakes by recurrent Neural network. *Forecasting*, *3*(1), 17–36. https://doi.org/10.3390/forecast3010002

Picozzi, M., Iaccarino, A. G., & Spallarossa, D. (2024a). The preparatory process of the 2023 Mw 7.8 Türkiye earthquake. *Scientific Reports*, *13*(1), 17853. https://doi.org/10.1038/s41598-023-45073-8

Picozzi, M., Iaccarino, A. G., Spallarossa, D., & Bindi, D. (2023). On catching the preparatory phase of damaging earthquakes: An example from central Italy. *Scientific Repports*, *2023*(1), 14403. https://doi.org/10.1038/s41598-023-41625-0

Picozzi, M., Spallarossa, D., Iaccarino, A. G., & Bindi, D. (2024b). Event-specific ground motion anomalies highlight the preparatory phase of earthquakes during the 2016–2017 Italian seismicity. *Communications Earth & Environment*, *5*(1), 289. https://doi.org/10.1038/s43247-024-01455-y

Ricci, T., Barberi, F., Davis, M. S., Isaia, R., & Nave, R. (2013). Volcanic risk perception in the Campi Flegrei area. *Journal of Volcanology and Geothermal Research*, *254*, 118–130. https://doi.org/10.1016/J.JVOLGEORES.2013.01.002

Ricciolino, P., Lo Bascio, D., & Esposito, R. (2024). *GOSSIP—database sismologico pubblico INGV. Osservatorio Vesuviano*. Istituto Nazionale Di Geofisica e Vulcanologia (INGV).

Rouet-Leduc, B., Hulbert, C., Lubbers, N., Barros, K., Humphreys, C. J., & Johnson, P. A. (2017). Machine learning predicts laboratory earthquakes. *Geophysical Research Letters*, *44*(18), 9276–9282. https://doi.org/10.1002/2017GL074677

Scotto di Uccio, F., Lomax, A., Natale, J., Muzellec, T., Festa, G., Nazeri, S., et al. (2024). Delineation and fine-scale structure of fault zones activated during the 2014–2024 unrest at the Campi Flegrei caldera (southern Italy) from high-precision earthquake locations. *Geophysical Research Letters*, *51*(12), e2023GL107680. https://doi.org/10.1029/2023GL107680

Shapiro, S. A., Dinske, C., Langenbruch, C., & Wenzel, F. (2010). Seismogenic index and magnitude probability of earthquakes induced during reservoir fluid stimulations. *The Leading Edge*, *29*(3), 304–309. https://doi.org/10.1190/1.3353727

Shapiro, S. A., Krüger, O. S., Dinske, C., & Langenbruch, C. (2011). Magnitudes of induced earthquakes and geometric scales of fluid-stimulated rock volumes. *Geophysics*, *76*(6). https://doi.org/10.1190/geo2010-0349.1

Silleni, A., Giordano, G., Isaia, R., & Ort, M. H. (2020). The magnitude of the 39.8 ka Campanian ignimbrite eruption, Italy: Method, uncertainties and errors. *Frontiers in Earth Science*, *8*, 543399. https://doi.org/10.3389/FEART.2020.543399

Tramelli, A., Convertito, V., & Godano, C. (2024). b value enlightens different rheological behaviour in Campi Flegrei caldera. *Communications Earth & Environment*, *5*(1), 275. https://doi.org/10.1038/s43247-024-01447-y

Tramelli, A., Giudicepietro, F., Ricciolino, P., & Chiodini, G. (2022). The seismicity of Campi Flegrei in the contest of an evolving long term unrest. *Scientific Reports*, *12*(1), 2900. https://doi.org/10.1038/s41598-022-06928-8

Tramelli, A., Godano, C., Ricciolino, P., Giudicepietro, F., Caliro, S., Orazi, M., et al. (2021). Statistics of seismicity to investigate the Campi Flegrei caldera unrest. *Scientific Reports*, *11*(1), 1–10. https://doi.org/10.1038/S41598-021-865066

Troise, C., De Natale, G., Schiavone, R., Somma, R., & Moretti, R. (2019). The Campi Flegrei caldera unrest: Discriminating magma intrusions from hydrothermal effects and implications for possible evolution. *Earth-Science Reviews*, *188*, 108–122. https://doi.org/10.1016/J.EARSCIREV.2018.11.007

Vanorio, T., Geremia, D., Landro, G. D., & Guo, T. (2025). The recurrence of geophysical manifestations at the Campi Flegrei caldera. *Science Advances*, *11*(18), 2067. https://doi.org/10.1126/SCIADV.ADT2067

Vanorio, T., & Kanitpanyacharoen, W. (2015). Rock physics of fibrous rocks akin to Roman concrete explains uplifts at Campi Flegrei caldera. *Science*, *349*(6248), 617–621. https://doi.org/10.1126/science.aab1292

Vanorio, T., Virieux, J., Capuano, P., & Russo, G. (2005). Three-dimensional seismic tomography from P wave and S wave microearthquake travel times and rock physics characterization of the Campi Flegrei Caldera. *Journal of Geophysical Research*, *110*(B3), 1–14. https://doi.org/10.1029/2004JB003102

Venegas-Aravena, P., & Zaccagnino, D. (2025). Large earthquakes are more predictable than smaller ones. *Seismica*, *4*(1). https://doi.org/10.26443/seismica.v4i1.1568

Woessner, J., & Wiemer, S. (2005). Assessing the quality of earthquake catalogues: Estimating the magnitude of completeness and its uncertainty. *Bulletin of the Seismological Society of America*, *95*(2), 684–698. https://doi.org/10.1785/0120040007

Zaccagnino, D., Vallianatos, F., Michas, G., Telesca, L., & Doglioni, C. (2024). Are foreshocks fore-shocks? *Journal of Geophysical Research: Solid Earth*, *129*(2), e2023JB027337. https://doi.org/10.1029/2023jb027337

Zollo, A., Maercklin, N., Vassallo, M., Iacono, D. D., Virieux, J., & Gasparini, P. (2008). Seismic reflections reveal a massive melt layer feeding Campi Flegrei caldera. *Geophysical Research Letters*, *35*(12). https://doi.org/10.1029/2008GL034242